

# Experimental and Numerical Investigations of Flow Confined in a Vertical Missile Launcher

F. Sourgen,<sup>\*</sup> J. Haertig,<sup>†</sup> and C. Rey<sup>‡</sup>

*French–German Research Institute of Saint-Louis, 68301 Saint Louis, France*

and

D. Baudin<sup>§</sup> and N. Getin<sup>¶</sup>

*MBDA France, 92358 Le-Plessis-Robinson, France*

DOI: 10.2514/1.37614

A supersonic underexpanded round jet issuing from a De Laval nozzle designed for Mach 3 was directed into a U-shaped launcher container. Studies on transient and steady flow in the container were carried out using two distinct methods. Differential interferometry and particle image velocimetry investigations were conducted to collect reliable data on high-speed flow inside the container. High-rate visualizations and particle image velocimetry measurements allowed us to capture the incoming shock wave during the transient phase and to determine the Reynolds stress tensor in the container's plane of symmetry during the steady phase. The measurements were compared to the unsteady Reynolds-averaged Navier–Stokes solution. The effect of confinement, the anisotropy of the Reynolds stresses in the turbulent jet layer, the strong large-scale oscillating and bursting jet behavior, as well as the multiple waves at the container exit turned out to be critical points for the unsteady Reynolds-averaged Navier–Stokes method.

## Nomenclature

$G$	=	Gladstone–Dale constant at 532.5 nm wavelength, $\text{m}^3 \cdot \text{kg}^{-1}$
$I$	=	intensity of light, 0–256 (gray scale)
$k$	=	turbulent kinetic energy, $\text{m}^2 \cdot \text{s}^{-2}$
$L_f$	=	horizontal integral turbulence length scale, mm
$L_g$	=	vertical integral turbulence length scale, mm
$N(\mathbf{r})$	=	number of PIV samples at current location
$P$	=	static pressure, Pa
$P_t$	=	total pressure, Pa
$P_{ti}$	=	stagnation pressure, Pa
$R_{ij}$	=	normalized spatial correlation coefficient
$\mathbf{r}$	=	current location in the flow, m
$T$	=	static temperature, K
$T_{ti}$	=	stagnation temperature, K
$t$	=	time, s
$t_n$	=	instant of PIV sample number $n$ , s
$u, u_1$	=	instantaneous velocity component along the $x$ axis, $\text{m} \cdot \text{s}^{-1}$
$\langle u \rangle$	=	mean value of the horizontal component of the velocity field, $\text{m} \cdot \text{s}^{-1}$
$u'_i$	=	fluctuation of the $i$ component of the velocity field, $\text{m} \cdot \text{s}^{-1}$
$\overline{u'_i u'_j}$	=	statistical Reynolds stresses, $\text{m}^2 \cdot \text{s}^{-2}$

$\langle u'_i u'_j \rangle$	=	temporal measurement of the Reynolds stresses, $\text{m}^2 \cdot \text{s}^{-2}$
$v, u_2$	=	instantaneous velocity component along the $y$ axis, $\text{m} \cdot \text{s}^{-1}$
$\langle v \rangle$	=	mean value of the horizontal component of the velocity field, $\text{m} \cdot \text{s}^{-1}$
$w, u_3$	=	instantaneous velocity component along the $z$ axis, $\text{m} \cdot \text{s}^{-1}$
$X$	=	horizontal coordinate in the PIV image, pixel
$x$	=	horizontal coordinate in the map laser sheet, m
$Y$	=	vertical coordinate in the PIV image, pixel
$y$	=	vertical coordinate in the map laser sheet, m
$z$	=	transverse coordinate, m
$\Delta X$	=	horizontal displacement between successive PIV images, pixel
$\Delta Y$	=	vertical displacement between successive PIV images, pixel
$\delta_{ij}$	=	Kronecker symbol
$\lambda$	=	wavelength, nm
$\mu_t$	=	dynamic eddy viscosity, $\text{kg} \cdot \text{m}^{-1} \cdot \text{s}^{-1}$
$\rho$	=	density, $\text{kg} \cdot \text{m}^{-3}$
$\varphi$	=	phase of the interferometer, rad

## I. Introduction

PREDICTION tools are necessary for vertical missile launchers as this kind of launcher is intended to equip military naval platforms. Such a launcher may be composed of several independent modules, each consisting of a missile nozzle and a U-shaped container. It is of prime importance that the main features of the flow confined in the container are predicted correctly, not only for the integrity of the container itself, but also for the systems around the missile.

Because of the ejection from the missile nozzle and the shape of the container, the investigation of such a flow covers the topic of supersonic impinging jet flows, which has been studied for the last decade in various configurations [1–5], mainly to study acoustic noise and interaction with lift surfaces in aeronautics. Although these configurations were very different from our topic, several numerical and experimental investigations pointed out that the critical feature of high-speed impinging jet flows is the formation of impingement-induced large-scale flow structures, which interact with the jet and make the flowfield particularly unsteady.

Received 20 March 2008; revision received 31 July 2008; accepted for publication 15 October 2008. Copyright © 2008 by the French–German Research Institute of Saint-Louis. Published by the American Institute of Aeronautics and Astronautics, Inc., with permission. Copies of this paper may be made for personal or internal use, on condition that the copier pay the \$10.00 per-copy fee to the Copyright Clearance Center, Inc., 222 Rosewood Drive, Danvers, MA 01923; include the code 0022-4650/09 \$10.00 in correspondence with the CCC.

<sup>\*</sup>Researcher, Aerodynamics Department, 5 rue du Général Cassagnou, Post Office Box 70034; frederic.sourgen@isl.eu. Member AIAA.

<sup>†</sup>Head of Aerodynamics and Ballistics Department, 5 rue du Général Cassagnou, Post Office Box 70034; jacques.haertig@isl.eu.

<sup>‡</sup>Engineer, Aerodynamics and Ballistics Department, 5 rue du Général Cassagnou, Post Office Box 70034; christian.rey@isl.eu.

<sup>§</sup>Research and Development Engineer, Aerodynamics and Performances Department, 1 avenue Réaumur; denis.baudin@mbda-systems.com.

<sup>¶</sup>Research and Development Engineer, Aerodynamics and Performances Department, 1 avenue Réaumur; nicolas.getin@mbda-systems.com.

Experimental investigations using particle image velocimetry (PIV) [6,7] highlighted these structures and allowed a better understanding of such flows. At the same time, numerical investigations using the large eddy simulation (LES) [8,9], or hybrid methods coupling the Reynolds-averaged Navier–Stokes (RANS) with LES methods, succeeded in capturing the main features of this kind of flow [5]. These numerical methods consist of modeling only the dissipative turbulence and of resolving the largest unsteady scales [10]. However, their efficiency requires a much smaller grid spacing than turbulent length scale, which usually incurs considerable computational costs [11,12]. Therefore, they are generally used for simple geometries, rarely for a complete simulation of an industrial system with multiple interacting objects.

In the case of a vertical missile launcher, the flow confined in the container represents only one part of the whole computation used for predicting the dynamics of the missile leaving the container. The missile itself has to be modeled in addition to the container, and the process of mesh adaptation to describe the move of the missile relative to the container consumes a major part of the computational resources. In addition, the real geometry has to be taken into account, which is much more complex than the basic geometries usually used with the RANS/LES coupled methods. Finally, the Reynolds number for the investigated flow is about  $1.4 \times 10^6$ . This value is considerably higher than the usual values for RANS/LES methods.

Under these conditions, an unsteady RANS approach (URANS) equipped with a turbulence model [13–16] has to be chosen. However, it is of prime importance that the inadequacies of this method for the precise case of a missile in a container are evaluated as well as the possible consequences for the system as a whole, and also the modifications of the code which can be made to avoid them. To answer these questions, a test case representative of the real flow in a container has been chosen and an experimental database using PIV and high-speed visualizations has been built. First, this database allows a better understanding of the physics of the flow in a vertical missile launcher. Second, it allows a useful comparison with numerical simulations.

This paper presents a complete description of the experimental approach and describes the critical features of the flow in the container during the transient phase, when the initial shock wave enters the container, and during the steady phase, when the flow is established in the container. The numerical method is also described and the results are compared to experiments during transient and steady phases. Finally, this paper presents a detailed discussion on the observed differences and it suggests some modifications to improve the numerical tool intended to simulate the real launch.

## II. Experimental Facilities

### A. Model of a Launcher and Stagnation Conditions

The geometry of the model must comply with a real container and missile scale factor while allowing the PIV investigation, that is, the width of the laser sheet. These constraints are taken in account by the U-shaped container shown in Fig. 1. Although it is, in fact, a vertical launcher, the nozzle axis is represented, from now on, as the horizontal  $x$  axis. The side, top, and bottom walls are made out of BK7 glass with a thickness of 30 mm and an optical quality of  $\lambda/5$ , as is the separation plate in order to let the laser sheet pass through.

The value of the stagnation pressure was set at 70 bars because this is a realistic value for a missile. However, the perfectly expanded jet stagnation pressure for the De Laval nozzle designed for Mach 3, shown in Fig. 1, is 36 bars. This means that underexpansion effects are to be expected, as observed in the case of freejets [17–20]. The stagnation temperature was set at 300 K. Obviously, this does not match the realistic temperature which is about 2500 K, but the time required to collect enough PIV samples for statistics implies that the temperature in the flow facility must remain lower than 350 K. Although the thermal and dynamic blending of turbulence models is of prime importance in propulsive jets [21], the work described in this paper is based on the dynamics inside the container.

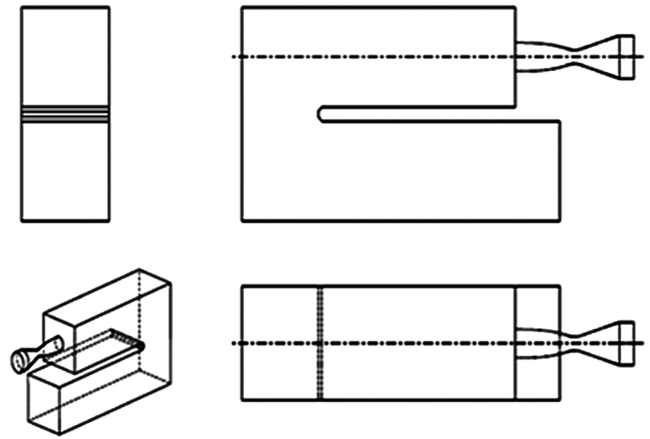


Fig. 1 Model of a module in a vertical launcher.

### B. Flow Study Facilities

Different facilities were used for the investigation of the transient and steady parts of the flow. In the case of the transient flow, stagnation conditions must be reached immediately (in a much shorter time than the characteristic transient time). For that purpose, a shock tube was used as a blowdown wind tunnel. While the fluid in the low-pressure tube was released into the container, the stagnation pressure was maintained for about 90 ms, which was wholly sufficient for the transient flow study (5 ms), but not enough to obtain more than one instantaneous PIV sample. An important point, especially for computation, was the working gas in the low-pressure tube, that is nitrogen released into the air.

In the case of the steady flow investigation, another facility was used. It was supplied by a compressor used for a blowdown wind tunnel which can operate for 60 s. This time, the stagnation pressure took a few seconds to reach its nominal value and air was used as working gas.

As seeding remains a critical point in the PIV technique, it may be useful to describe the particle generator used in both facilities. Although several kinds of generators and liquid droplets were tested, the best results for this study were obtained with the solid particle generator shown in Fig. 2. The principle is quite simple: a circle of nozzles creates a vortex which scatters and absorbs particles toward the exit. Particles have a size of  $0.1 \mu\text{m}$ . This generator, designed at

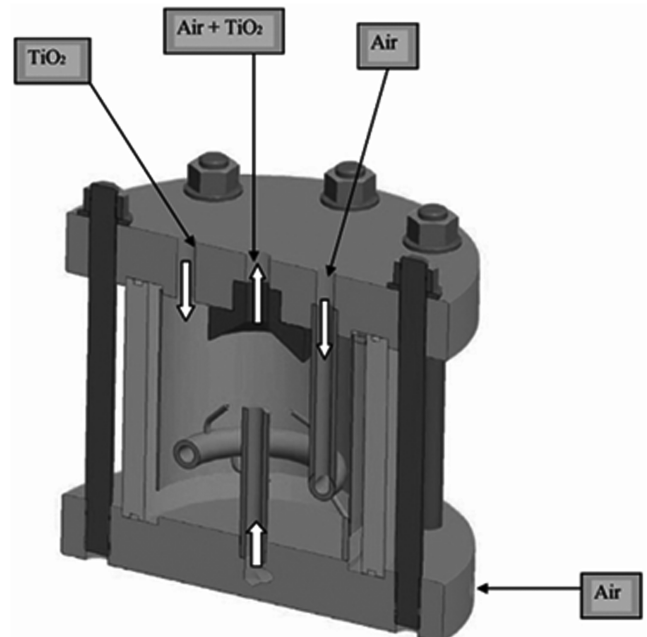


Fig. 2 Solid particle generator cross section.

the French–German Research Institute of Saint-Louis, has been used successfully in the PIV technique for several years [22–24] and a more complete description can be found in [25].

### III. Experimental Setup and Postprocessing

#### A. Experimental Setup

High-rate visualizations were performed only for the transient flow study. Differential interferometry is used and the experimental setup for the shock tube is shown in Fig. 3. This well-known technique used since the 1960s is, among the “refraction index sensitive techniques,” the most sensitive to refractive index gradients in the flow [26]. Visualizations up to 30 kHz from the very beginning of the flow were compared to computation.

PIV was used to measure the instantaneous velocity field in the planar symmetry cross section of the model during the transient and steady parts of the flow. The PIV experimental setup is shown in Fig. 4 in the case of the steady flow study facility. The flow was seeded upstream from the nozzle using the small-sized solid particle generator shown in Fig. 2. The calibration of the seeding was carried out as follows: as particles were introduced upstream from the nozzle using an overpressure, several preliminary blowdowns allowed the adequate pressure in the generator relative to the stagnation pressure to be determined. The optimal overpressure in the generator was

10 bars. As the stagnation pressure was very stable, the quality of seeding was maintained during a blowdown.

The particles were illuminated by two consecutive laser sheets produced by a double pulse laser YAG (532.5 nm) and separated by a 1  $\mu$ s time interval. The energy of double impulses was 150 mJ each, with a duration of 5 ns and a rate of 3 Hz. The light scattered by the particles located in the laser sheet was collected using two side-by-side double-frame charge-coupled device (CCD) cameras. In this way, the velocity field was obtained instantaneously in the upper part of the flow. The same was done for the bottom part of the flow by moving the double camera system down. The CCD cameras were 1280  $\times$  1024 pixels Sharp ProVision cameras.

The most likely displacement of particles was determined by computing the spatial cross correlation between the local analysis windows in the consecutive images, then dividing by the time interval to get the velocity vector in each interrogation window. The displacement vector was computed with an accuracy of about 0.1 pixel. Given the magnification factor and time interval, this corresponded to an accuracy of 10 m/s for the instantaneous speed vector.

#### B. PIV Data Reduction for Steady Flow Investigation

In the case of the steady flow investigation, more than 100 PIV samples were generated during blowdowns so that, in addition to the classical spatial cross-correlation computation, an automatic best-sample selective algorithm was developed.

PIV image pairs were analyzed by the cross correlation of small interrogation windows centered on the nodes  $X, Y$  of a grid covering the field of interest. The correlation algorithm gave the most likely displacement  $\Delta X, \Delta Y$  of particles and an estimate of the quality of the correlation function. Moreover, a high-pass filter for spatial frequencies was applied to increase the quality of the measurements in regions of inhomogeneous seeding. An iterative process was used to reduce the size of the interrogation windows and to move them from the previous estimated  $\Delta X, \Delta Y$  displacement. The best estimate of  $\Delta X, \Delta Y$  at  $X, Y$  was obtained by selecting the result of the smaller interrogation windows with a minimum quality criterion imposed. Then the displacements  $\Delta X, \Delta Y$  were achieved with a better accuracy than 0.1 pixel. Furthermore, temporal correlations were determined from the best PIV samples using the following Eq. (1):

$$\langle u'_i u'_j \rangle(\mathbf{r}, t) = \frac{1}{N(\mathbf{r})} \sum_{n=1}^{N(\mathbf{r})} u_i(\mathbf{r}, t_n) \times u_j(\mathbf{r}, t_n) - \left( \frac{1}{N(\mathbf{r})} \sum_{n=1}^{N(\mathbf{r})} u_i(\mathbf{r}, t_n) \right) \times \left( \frac{1}{N(\mathbf{r})} \sum_{n=1}^{N(\mathbf{r})} u_j(\mathbf{r}, t_n) \right) \quad (1)$$

The ergodicity theorem for steady turbulence was used to identify the temporal and statistical means, hence the Reynolds stress tensor. A most important criterion for a correct estimate is the need to have a sufficient number of samples so that the observation duration is much greater than the temporal turbulence scale. As shown in Fig. 5, the number of samples amounted to about 100. Using an acquisition rate equal to 3 Hz, the observation duration was about 30 s which is sufficient [27].

#### C. Integral Turbulence Length Scales

The exact decomposition of the turbulence would need a proper orthogonal decomposition process from 3-D samples. However, a good estimate of the biggest turbulence structures can be extracted using a spatial correlation process similar to that usually employed in the case of homogeneous isotropic turbulence [27]. The normalized spatial correlation coefficients are determined from PIV samples using Eq. (2). Then, estimates of the longitudinal and the transverse integral turbulence length scales are obtained by integration of the correlation coefficient, according to Eqs. (3) and (4), respectively,

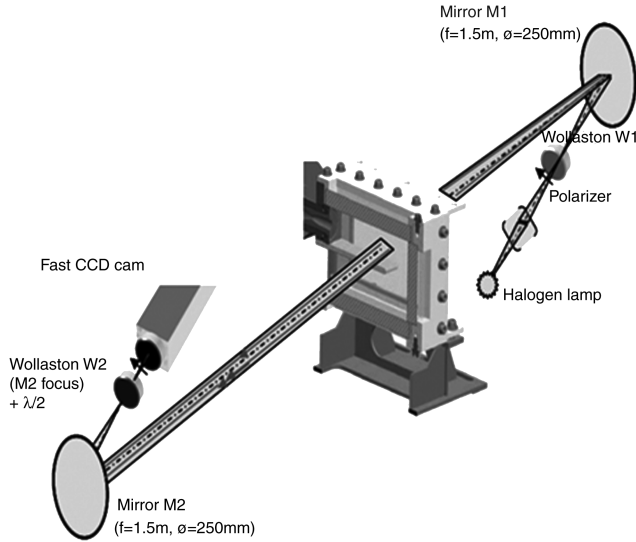


Fig. 3 Visualization setup.

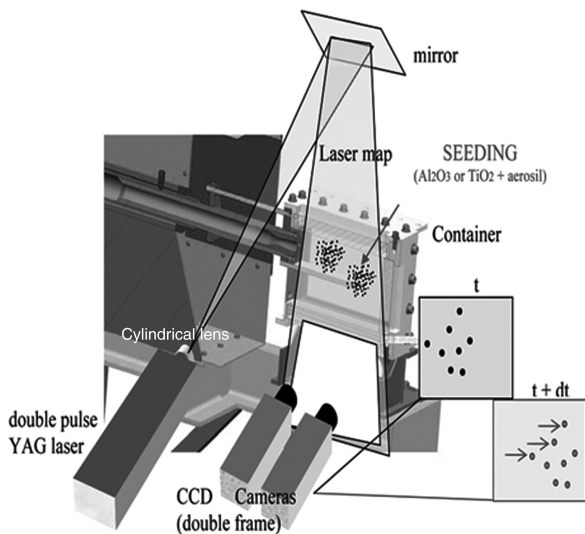


Fig. 4 PIV setup.



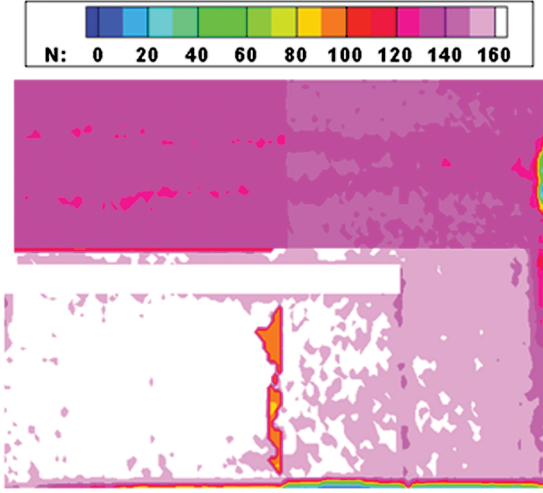


Fig. 5 Number of selected PIV samples in the planar symmetry cross section of the container.

$$R_{ij}(\mathbf{r}, \mathbf{r}') = \frac{\langle u'_i(\mathbf{r}) \rangle \langle u'_j(\mathbf{r}') \rangle}{\sqrt{\langle u'_i(\mathbf{r})^2 \rangle \langle u'_j(\mathbf{r}')^2 \rangle}} \quad (2)$$

$$L_f(\mathbf{r}) = \frac{1}{2} \int_{-\infty}^{+\infty} R_{uu}(\mathbf{r}, \mathbf{r} - x\mathbf{u}_x) dx \quad (3)$$

$$L_g(\mathbf{r}) = \frac{1}{2} \int_{-\infty}^{+\infty} R_{uu}(\mathbf{r}, \mathbf{r} - y\mathbf{u}_y) dy \quad (4)$$

The integral turbulence length scales are shown in Figs. 6a and 6b. It can be observed that, except in the potential core of the jet, these scales are particularly high: the maximum value is around 14 mm for the longitudinal scale. This information is particularly useful to prepare a numerical simulation and to build a mesh.

#### IV. Computational Method

Unsteady Reynolds-averaged Navier–Stokes numerical investigations have been carried out using Flusepa, a software developed by ASTRIUM ST and especially dedicated to aerospace computations. One of the main strengths of Flusepa is an adaptive time stepping, which means that even if the smallest time step is  $10e-9$  s, other cells (much more numerous in the computational domain) are computed with their own acceptable time step to comply with the Courant number criterion, which means significant

computational cost savings. However, the computational cost remains high: around two weeks of CPU with four Xeon 3 GHz processors for a 20 ms simulation duration in an openMP-type parallelization of the code.

The code also uses a Godunov scheme, more precise than the more widely used Roe schemes which roughly solve the Riemann problem. Here the code solves the Riemann problem exactly, using a monotone upstream-centered scheme for conservation laws (MUSCL) approach for the reconstruction of variables, which allows a second-order spatial accuracy on regular grids [28,29].

A detailed study was conducted in 2007 to examine the influence of grid refinements on numerical results [30]. The mesh presented here is sufficiently fine for URANS computation, as the results do not change significantly with grid refinement. This mesh was built using ICEM-CFD 11.0 (ANSYS) and is a structured grid consisting of 855,000 hexahedral elements, as shown in Fig. 7. The minimum face angle is 30 deg, the maximum face angle is 150 deg, and the first node

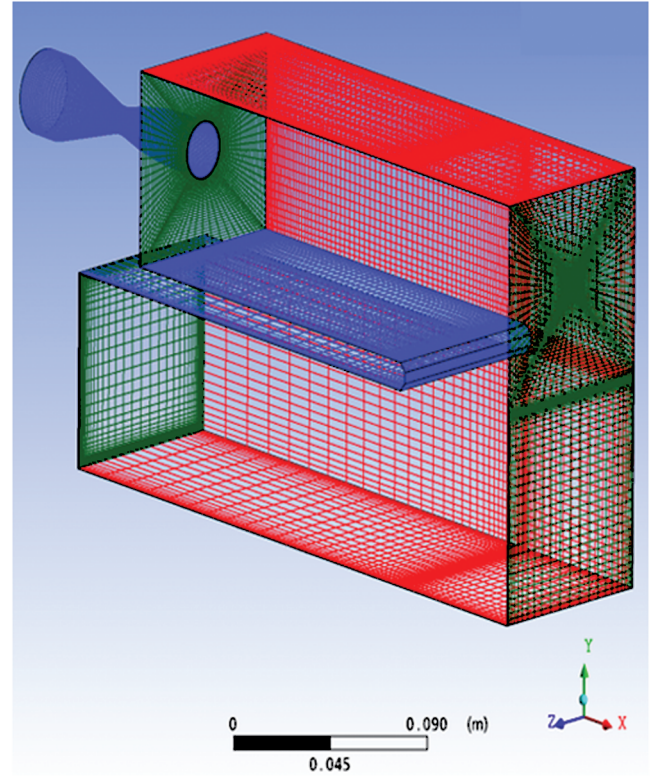
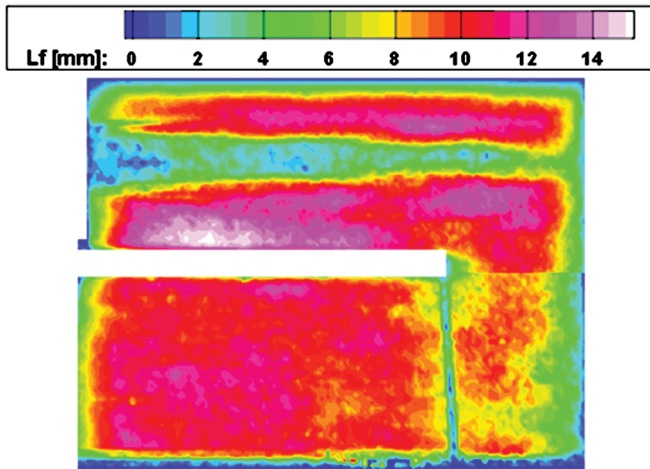
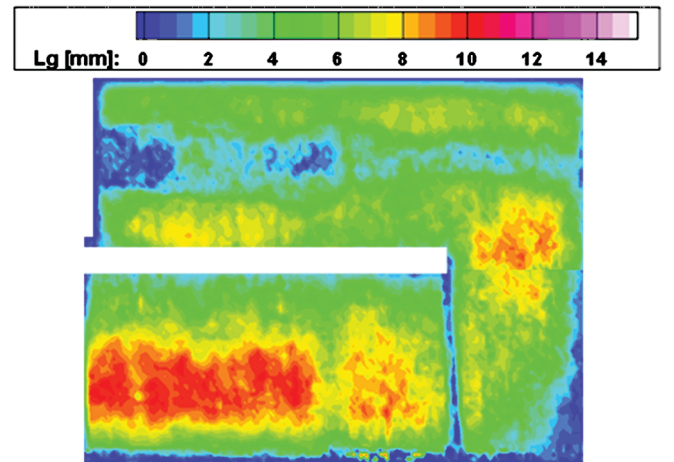


Fig. 7 Mesh.



a)



b)

Fig. 6 a) Estimate of the longitudinal integral turbulence length scale; b) estimate of the vertical integral turbulence length scale.



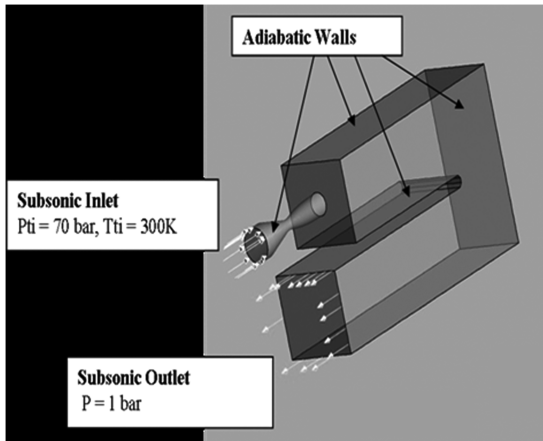
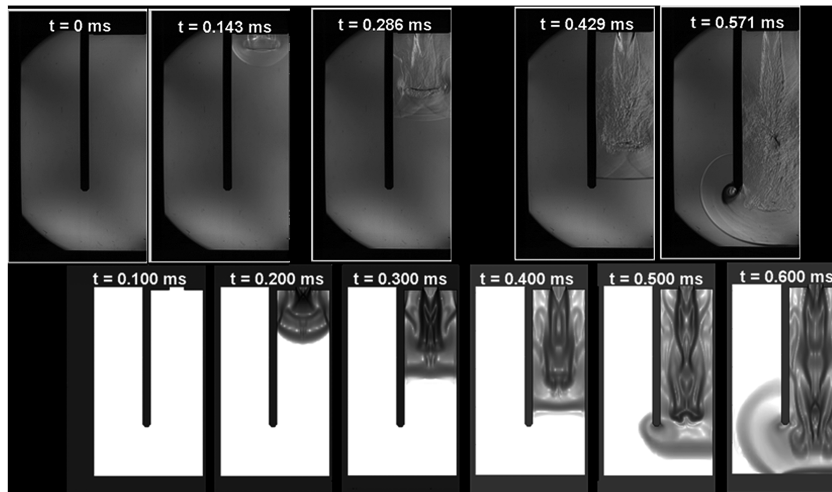


Fig. 8 Boundary conditions.

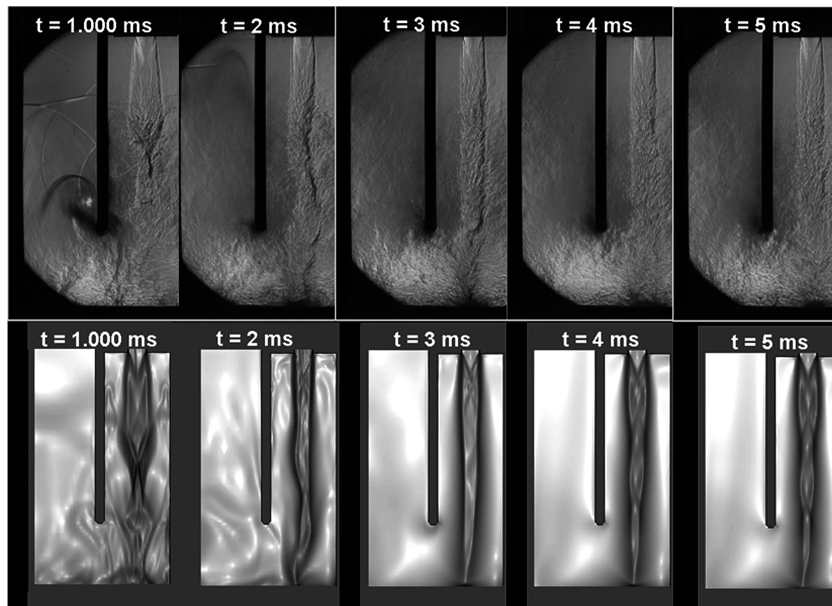
at the wall is  $50 \mu\text{m}$  from the wall. With regard to Figs. 6a and 6b the length of the cells in the impact region is lower than one-tenth of the measured longitudinal integral turbulence length scale.

Boundary conditions are shown in Fig. 8. A subsonic inlet boundary condition was applied upstream from the nozzle. The stagnation pressure was specified to be equal to 70 bars and the stagnation temperature was equal to 300 K. The turbulence kinetic energy at the inlet was equal to  $0.001 \text{ m}^2/\text{s}^2$  and the dissipation rate amounted to  $1000 \text{ m}^2/\text{s}^3$ . At the outlet, a subsonic nonreflective boundary condition was applied and only the total pressure was specified to be 1 bar. An adiabatic wall boundary condition was used for each wall in the container and for the nozzle.

To match experiments, computations were two-species simulations: the computation domain was initially filled in with still air, considered to be a compressible ideal mixture, but the incoming gas was nitrogen. This point did not matter for the steady part of the flow, but it was of prime importance for the incoming shock wave.



a)



b)

Fig. 9 a) Comparison between visualization and URANS computation; b) comparison between visualization and URANS computation.

The turbulence model used is a high Reynolds number  $K-\varepsilon$  of the Jones–Launder model type, equipped with restrictive criteria for the turbulent production term [28,29]. In the case of the (U)RANS computations and first-order turbulence models, the Reynolds stress tensor is defined from the eddy viscosity, mean velocity field, and turbulent kinetic energy by the compressible Boussinesq model [27]. Turbulent stresses were extracted using the following Eq. (5):

$$-\rho \overline{u'_i u'_j} = \mu_t \left( \frac{\partial \bar{u}_i}{\partial x_j} + \frac{\partial \bar{u}_j}{\partial x_i} \right) - \frac{2}{3} \rho \bar{k} \delta_{ij} - \frac{2}{3} \mu_t \frac{\partial \bar{u}_i}{\partial x_i} \delta_{ij} \quad (5)$$

## V. Transient Flow Experimental and Numerical Results

### A. Incoming Shock Wave

The shock wave coming into the container was visualized using differential interferometry at a frequency of 7 kHz. As the light beam was vertically separated by the Wollaston biprism 1 (Fig. 3), the intensity on the fast CCD camera had the shape described by the following Eqs. (6) and (7):

$$I(X, Y) = I_{\min} + (I_{\max} - I_{\min}) \sin^2(\varphi(X, Y) + \varphi_0) \quad (6)$$

$$\varphi(X, Y) = \frac{2\pi}{\lambda} \int_{-\infty}^{+\infty} \frac{1}{G} \frac{\partial \rho}{\partial y} ds \quad (7)$$

Indeed, the reference phase as well as the minimum and maximum values of intensity varied slowly according to time and position, due to the limited optical quality of glass ( $\lambda/5$ ) and the constraints exerted. Therefore, computational fluid imaging could not be satisfactorily used for a further comparison with simulations. The comparison was made using the logarithm of the symmetry plane density gradient obtained from the simulation, as given in Eq. (8):

$$\log \nabla \rho = \log \left( \left| \frac{\partial \rho}{\partial y} \right| \right) \quad (8)$$

The only justification for using a 2-D quantity, while the signal depends on the whole 3-D field, is that the flow remains rather axisymmetrical, and the main contributions are located in the plane of symmetry because the contributions on both sides of the plane of symmetry have opposite effects on the “ray deflection quantity” in Eq. (7).

A comparison between visualizations and URANS results as a function of time are shown in Figs. 9a and 9b. The visualizations are shown in the upper parts of the figures. Very good agreement is found

between the URANS computation and the visualizations of the dynamics of the incoming shock wave and secondary waves formed in the container. The thickness and numerical diffusion of shock waves in the computation are due to grid spacing, but the location of multiple waves as a function of time matches the visualizations particularly well. Both the computation and experiment indicate that the transient flow duration is about 5 ms. However, the visualizations show that the jet keeps oscillating strongly and bursting toward the end of the transient flow, whereas the URANS computation reaches a steady state.

Another noticeable characteristic is that, because of confinement, at the end of the transitory phase the jet is not very underexpanded at the nozzle exit in the experiment, despite the high stagnation pressure of 70 bars which would correspond to a pressure ratio almost equal to 2 in the case of an open flow. However, several Mach cells clearly appear in the URANS computation. Even if they are not as large as would be the case if the jet were a free one, the effect of the confinement is not perfectly taken into account by the computation. An overdiffusion of the turbulence in the computation may prevent the transport of the fluid back to the nozzle exit, whereas in reality this transport interacts strongly with the jet at the exit of the nozzle.

### B. Transient Flow Velocity Field

Particle image velocimetry recordings can be performed only once during the transitory phase, mainly due to the maximum rate of the double impulsion laser, but the experiments are well reproducible and the laser sheet and the camera can be triggered to measure velocity at an instant which has been chosen in advance. In this way, Fig. 10a shows the incoming shock wave at the nozzle exit and Fig. 10b shows the corresponding horizontal velocity component. Blanked values correspond to insufficient seeding. The PIV instantaneous velocity field allows quantitative comparisons between the experiment and the URANS computation of the transient flow at different times and different locations. Figures 10b and 10c allow the comparison of results at the nozzle exit when the shock wave comes into the container. Figures 11b and 11c allow the comparison in the impact region at the end of the transient regime.

Figure 10c shows that the horizontal velocity component upstream from the shock wave is underestimated and that the incoming shock wave appears thick in URANS computations. Both results are due to the fact that the grid is coarse in this region. In fact, a better description of the incoming shock wave at every instant would need a grid refinement in all parts of the container, which could be attained using an adaptative mesh process but at considerable computational cost. Moreover, Fig. 10 shows also that the location of the shock as a function of time matches well with the experiment, and Fig. 11 shows that there is again good agreement at the end of the transitory phase.

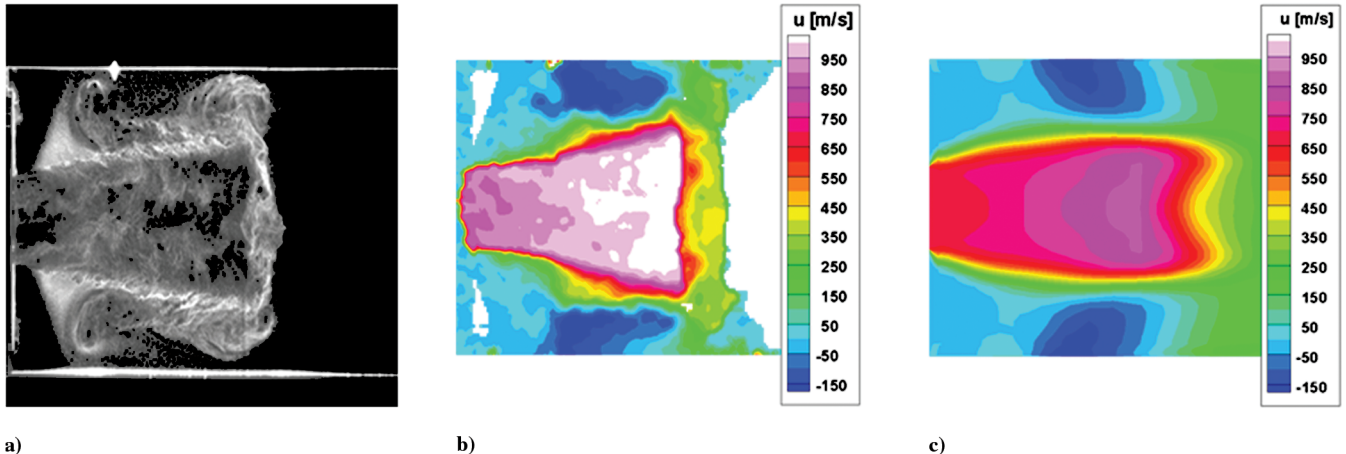


Fig. 10 a) PIV frame of the incoming shock wave ( $t = 0.3$  ms); b) PIV measured instantaneous horizontal velocity component ( $t = 0.3$  ms); and c) URANS result ( $t = 0.3$  ms).

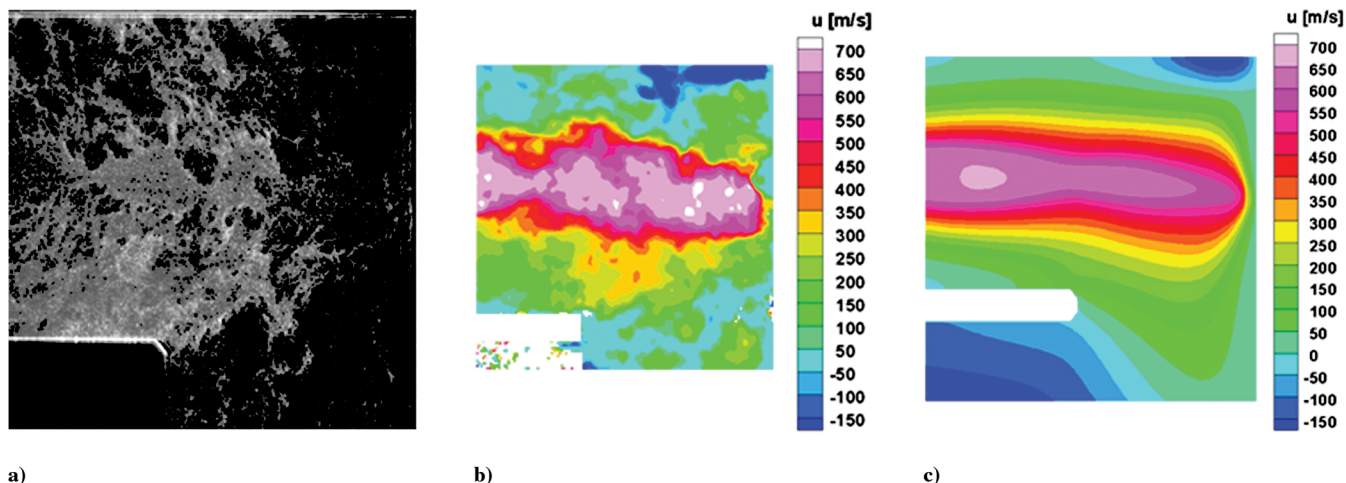


Fig. 11 a) PIV frame in the impact region ( $t = 20$  ms); b) PIV measured instantaneous horizontal velocity component ( $t = 20$  ms); and c) URANS result ( $t = 20$  ms).

Furthermore, Figs. 12a and 12b show there is now almost no difference anymore in the URANS computation between the flow at 15 ms and the flow at 20 ms. This means that the URANS computation has reached a steady state. This is a most important point because it means the turbulence became steady in the computation at the end of the transitory phase, so that a further comparison with PIV measurements during the steady phase does not need to involve URANS samples; it can be made simply using the result at 20 ms. In addition, it should be noted that the fact that the turbulence became steady in the computation may be related to an overestimate of the eddy viscosity by the turbulence model. Therefore, for the steady phase and for further computations with some modifications of the turbulence model, the URANS approach should be kept instead of RANS.

## VI. Steady Flow Experimental and Numerical Results

### A. Mean Velocity Field

The streamlines and mean horizontal component of the velocity field computed and measured in the symmetry plane of the container are shown in Figs. 13a and 13b, respectively. Similarly the mean vertical component is shown in Figs. 14a and 14b. It should be noted that PIV measurements are a little distorted precisely in the region under the extremity of the separation plate due to the wedge deflection of the laser sheet.

For a stagnation pressure equal to 70 bars, Fig. 13a shows that the jet is underexpanded in the computation at the nozzle exit. Mach cells can be particularly observed in Fig. 14a as there are three successive

changes in the vertical velocity component direction. However, in the experiment, the Mach cells are much smaller than in the URANS computation which behaves more like a free underexpanded jet at the nozzle exit. It should be noted that, in the experiment, the jet is effectively slightly underexpanded. This is highlighted by the PIV frame shown in Fig. 14c: a small nitrogen liquid cell can be observed close to the nozzle exit, which is related to the decrease in the temperature due to expansion. But this phenomenon occurs very infrequently during a blowdown, and only a few PIV frames allow its detection. That is why it is not highlighted by statistical means, as Fig. 14b, for instance.

Furthermore, all pictures show that, in the experiments, impact is on average centered on the nozzle axis, whereas in the URANS computations it is located at about one nozzle exit radius under the nozzle axis.

Figures 13a and 13b show that, in the experiment, a recirculating region spreads back to the nozzle exit, whereas it stops a few nozzle exit diameters before in the case of the URANS computations. The consequence of this lack of back advection of fluid in the simulations is a strong recirculating zone at the end of the jet, causing the off-centering of the jet compared with the experiment.

Finally Fig. 13a emphasizes another important point: in the URANS computations the mean horizontal velocity component at the exit of the container is, in absolute value, definitely higher than in the experiments. The URANS computation predicted around 200 m/s container exit horizontal speed, whereas it was around 170 m/s in the experiment. In the next section an interpretation is suggested, based on Reynolds stress comparisons.

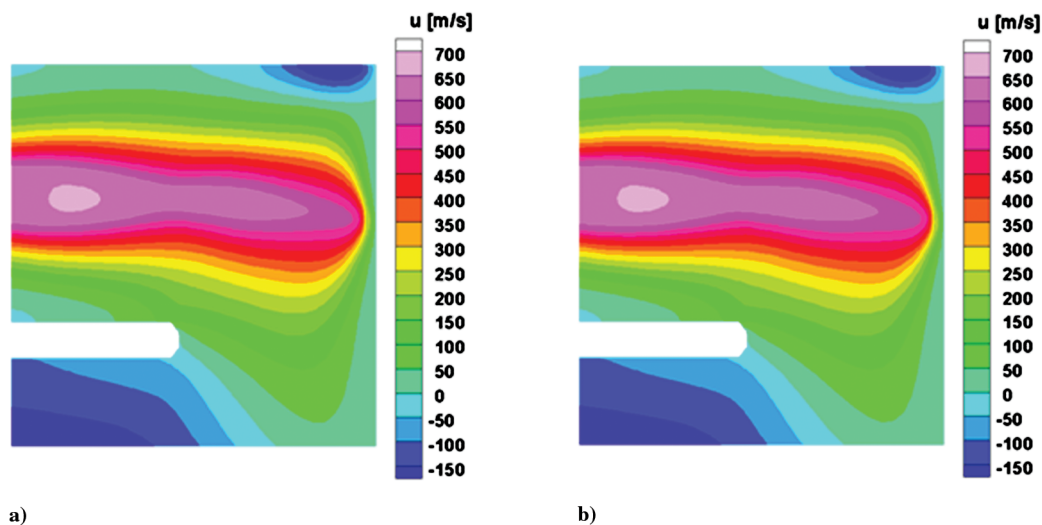


Fig. 12 a) URANS result at  $t = 15$  ms; b) URANS result at  $t = 20$  ms.



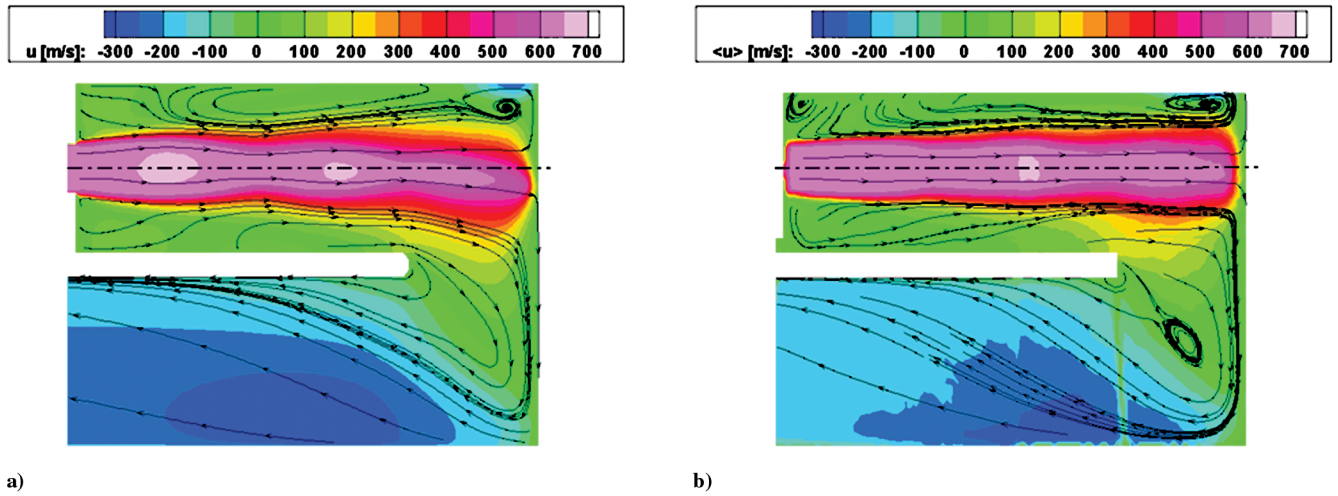


Fig. 13 a) URANS result at 20 ms; b) PIV mean horizontal velocity component.

### B. Reynolds Stress Tensor and Turbulent Kinetic Energy

The fluctuations  $\sqrt{\overline{u'^2}}$  and  $\sqrt{\overline{v'^2}}$  of the Reynolds stress tensor in the symmetry plane of the container and for a stagnation pressure equal to 70 bars are shown in Figs. 15 and 16, respectively. The element  $\overline{u'v'}$  of the Reynolds stress tensor is pictured in Fig. 17 and the turbulent kinetic energy is shown in Fig. 18. As only the horizontal and vertical components of the velocity vector in the symmetry plane have been

measured, the experimental turbulence kinetic energy is obtained by writing  $\overline{w'^2} = \overline{v'^2}$ , which is often used in the case of jet flows.

In Figs. 15 and 16, a strong anisotropy of the Reynolds stresses can be observed in the turbulent jet layer in the experiment, and this cannot be reproduced in the URANS computation because, by construction, the eddy viscosity model produces isotropic Reynolds stresses. Moreover, Fig. 17 points out that the transverse stress  $\overline{u'v'}$  is

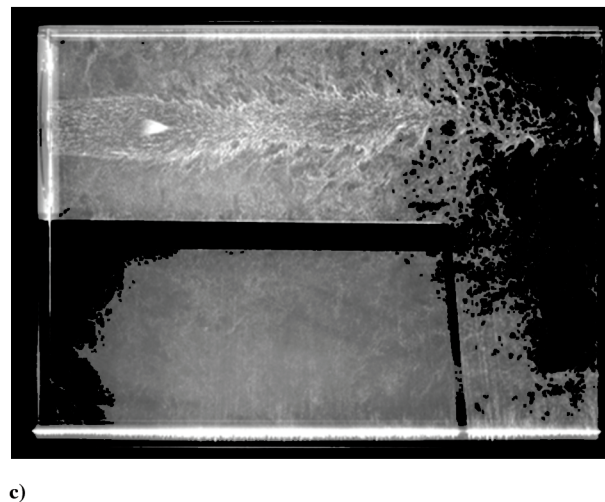
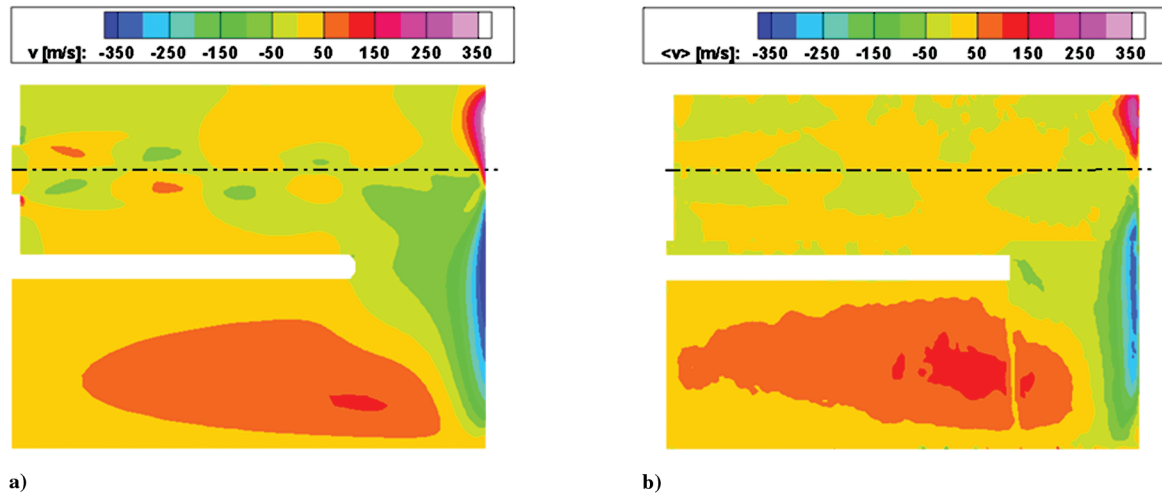


Fig. 14 a) URANS result at 20 ms; b) PIV mean vertical velocity component; and c) PIV frame during the steady phase.

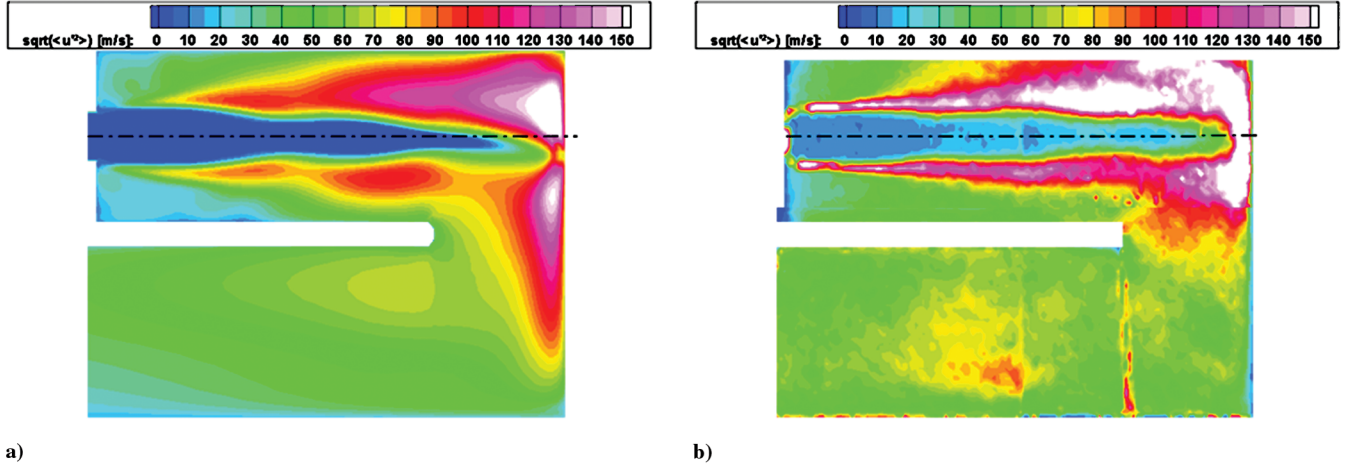


Fig. 15 a) URANS at  $t = 20$  ms; b) horizontal fluctuation of the velocity from PIV samples.

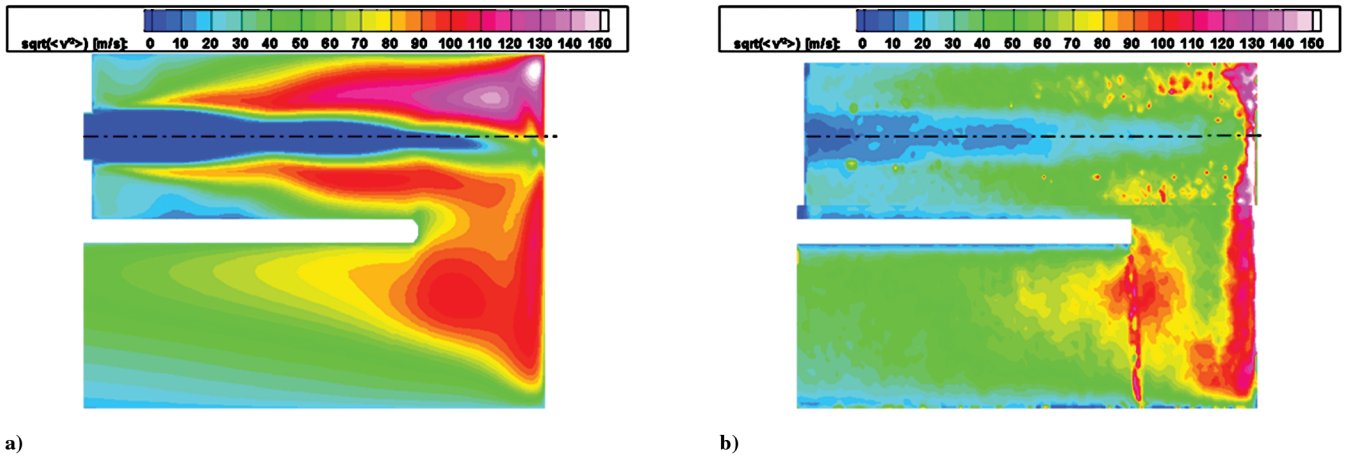


Fig. 16 a) URANS at  $t = 20$  ms; b) vertical fluctuation of the velocity from PIV samples.

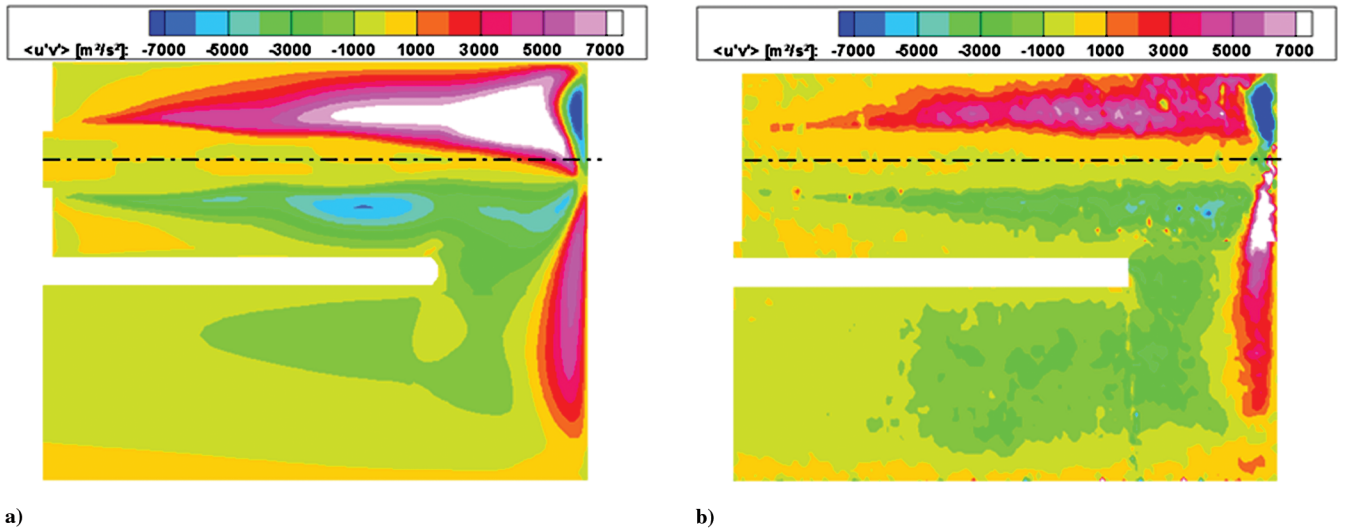


Fig. 17 a) URANS result at  $t = 20$  ms; b) transverse fluctuation of the velocity from PIV samples.

overestimated in the URANS computation, compared with the experimental results. This is due to an overproduction of shear turbulence in the jet layer. These are general results on the jet flow and the inability of eddy-viscosity-based models to correctly describe the turbulence in the jet shear layer.

A result of more concern is that, in the same pictures but at the impacted wall location, the experimental Reynolds stress levels are

greater than in the URANS solution. These high levels are due to the fact that the jet has kept oscillating and bursting long after the end of the transitory phase. Now these fluctuations cannot be correctly estimated in the URANS computation by an eddy-viscosity-based turbulence model, because the latter gives a diffusive character, fit to small scales, to large-scale phenomena whose origin is the nonlinear advection in Navier–Stokes equations.

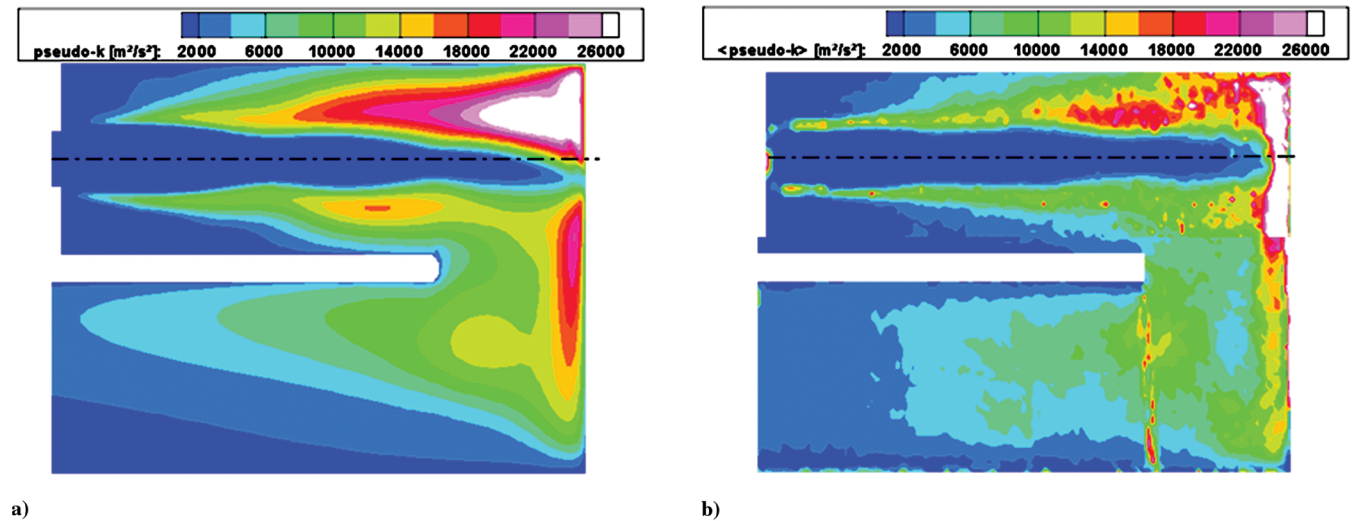


Fig. 18 a) URANS at  $t = 20$  ms; b) pseudokinetic energy from PIV samples.

In Figs. 15 and 16, in the bottom part of the impacted wall, an isotropic behavior along the wall has again been obtained by the URANS computation, whereas in the experiment the vertical fluctuations are much greater than the horizontal ones. This behavior is similar to the anisotropy observed in wall jet flows.

A more nonacademic result can be observed in Fig. 15b. Indeed, strong horizontal fluctuation levels were measured in the bottom part of the container, which are not even predicted by the URANS computation. As vertical fluctuations in Fig. 16b remained small in this location, multiple shock waves are likely to have occurred in this transonic region. This is another flow case where the description by the URANS method is known to be difficult. Consequently, as pointed out in the previous section, the horizontal velocity component at the container exit was overestimated by the URANS computation.

## VII. Conclusions

Studies on transient flow showed that the incoming shock wave and the jet structure evolution during the first milliseconds can be successfully predicted using the unsteady Reynolds-averaged Navier–Stokes method. Except for the numerical diffusion of shock waves due to grid spacing, the dynamics of the flow has been solved well in time and space, which is a very important point for the future simulation of the real launch.

However, the investigation during the steady phase showed several important differences between the experiment and the computation. First, the expansion of the jet layer is faster in the computation than in the experiment, and the jet is more underexpanded in the computation. This is due to the fact that eddy-viscosity-based models describe turbulence using a diffusive formulation, adequate for isotropic dissipative turbulence scales, but not for anisotropic and large-scale transport such as a turbulent jet layer. However, the behavior of the jet at the nozzle exit is of prime importance for missile surrounding systems and the simulation has to be improved. As grid refinement in the jet layer to allow the use of the LES/RANS methodology would involve prohibitive computational costs for the whole system simulation, the efforts should consist of either modifying the parameters of the turbulence model, or in testing second-order models.

Secondly, the large-scale back advection of fluid, due to impingement, was underestimated by the URANS computation, which reached a steady state at the end of the transient phase, whereas the jet continued to oscillate along the impacted wall. These large-scale structures come back to the nozzle and interact with the exit of the jet, so that it is again a point of prime importance for the missile. The origin of this large-scale advection is located in the impingement area and the corresponding turbulence scale is wide, about 15 mm in the horizontal direction. The fact that the recirculation zone above the jet, related to the above-mentioned large-scale structures, does not

reach the nozzle exit, seems to show that the eddy viscosity is overestimated by the turbulence model. That is why one solution to improve the numerical tool would be to decrease the eddy viscosity, by decreasing the Bradshaw constant, for instance.

## Acknowledgment

We thank the French Ministry of Defense for supporting the current work under Contract DGA/DSA/UM MID No. 05.70.129.00.470.75.96.

## References

- [1] Elavarasan, R., Venkatakrishnan, L., Krothapalli, A., and Lourenco, L., "A PIV Study of a Supersonic Impinging Jet," *Journal of Visualization*, Vol. 2, Nos. 3, 4, 2000, pp. 213–221.
- [2] Henderson, B., "The Connection Between Sound Production and Jet Structure of the Supersonic Impinging Jet," *Journal of the Acoustical Society of America*, Vol. 111, No. 2, 2002, pp. 735–747. doi:10.1121/1.1436069
- [3] Kim, S. I., and Park, S. O., "Oscillatory Behavior of Supersonic Impinging Jet Flows," *Shock Waves*, Vol. 14, No. 4, 2005, pp. 259–272. doi:10.1007/s00193-005-0270-9
- [4] Krothapalli, A., Rajkuperan, E., Alvi, F., and Lourenco, L., "Flow Field and Noise Characteristics of a Supersonic Impinging Jet," *Journal of Fluid Mechanics*, Vol. 392, 1999, pp. 155–181. doi:10.1017/S0022112099005406
- [5] Arunajatesan, S., and Sinha, N., "Large Eddy Simulations of Supersonic Impinging Jet Flow Fields," AIAA Paper 2002-4287, 2002.
- [6] Raffel, M., Willert, C. E., and Kompenhans, J., *Particle Image Velocimetry. A Practical Guide*, Springer-Verlag, Berlin, 1998.
- [7] Schröder, A., and Willert, C. E., *Particle Image Velocimetry. New Developments and Recent Applications*, Topics in Applied Physics, Vol. 112, Springer, Berlin, 2008, ISBN: 978-3-540-73527-4.
- [8] Bogey, C., Bailly, C., and Juvé, D., "Computation of the Sound Radiated by a 3-D Jet Using Large Eddy Simulation," AIAA Paper 2000-2009, 2000.
- [9] Lupoglazoff, N., Rahier, G., and Vuillot, F., "Application of the CEDRE Unstructured Flow Solver to Jet Noise Computations," *1st European Conference for Aerospace Sciences (EUCASS)*, Central Aerohydrodynamic Institute, Moscow, Russia, 2005.
- [10] Speziale, C. G., "Turbulence Modeling for Time-Dependent RANS and VLES: A Review," *AIAA Journal*, Vol. 36, No. 2, 1998, pp. 173, 184. doi:10.2514/2.7499
- [11] Menter, F. R., and Egorov, Y., "A Scale-Adaptive Simulation Model Using Two-Equation Models," AIAA Paper 2005-1095, 2005.
- [12] Egorov, Y., and Menter, F. R., "Development and Application of SST-SAS Turbulence Model in the DESIDER Project," AIAA Paper 2005-1095, 2007.
- [13] Menter, F. R., "Two-Equation Eddy-Viscosity Turbulence Models for Engineering Applications," *AIAA Journal*, Vol. 32, No. 8, 1994, pp. 1598, 1605. doi:10.2514/3.12149



- [14] Béchara, W., Lafon, P., Bailly, C., and Candel, S., "Application of a  $k-\varepsilon$  Model to the Prediction of Noise for Simple and Coaxial Free Jets," *Journal of the Acoustical Society of America*, Vol. 97, No. 6, 1995, pp. 3518, 3531.  
doi:10.1121/1.412438
- [15] Turpin, G., and Troyes, J., "Validation of a Two-Equation Turbulence Model for Axisymmetric Reacting and Non-Reacting Flows," AIAA Paper 2000-3463, 2000.
- [16] Wilcox, D. C., *Turbulence modeling for CFD*, DCW Industries Inc., La Canada, CA, 1993, ISBN: 0-963051-0-0.
- [17] Tam, C. K. W., Jackson, J. A., and Seiner, J. M., "A Multiple-Scales Model of the Shock-Cell Structure of Imperfectly Expanded Supersonic Jets," *Journal of Fluid Mechanics*, Vol. 153, 1985, pp. 123, 149.  
doi:10.1017/S0022112085001173
- [18] Tam, C. K. W., "Supersonic Jet Noise Generated by Large Scales Disturbances," *Journal of Sound and Vibration*, Vol. 38, 1975, pp. 51, 79.  
doi:10.1016/S0022-460X(75)80020-4
- [19] Wilkes, J. A., Glass, C. E., Danehy, P. M., and Nowak, R. J., "Fluorescence Imaging of Underexpanded Jets and Comparison with CFD," AIAA Paper 2006-910, 2006.
- [20] McDaniel, J. C., Glass, C. E., Staack, D., and Miller, C. G., "Experimental and Computational Comparison of an Underexpanded Jet Flowfield," AIAA Paper 2002-0305, 2002.
- [21] Thibert, J. J., Arnal, D., and Moin, "A Review of ONERA Aerodynamic Research in Support of a Future Supersonic Transport Aircraft," *Progress in Aerospace Sciences*, Vol. 36, 2000, pp. 581, 627.  
doi:10.1016/S0376-0421(00)00010-5
- [22] Haertig, J., Havermann, M., Rey, C., and George, A., "Particle Image Velocimetry in Mach 3.5 and 4.5 Shock Tunnel Flows," *AIAA Journal*, Vol. 40, No. 6, 2002, pp. 1056–1060.  
doi:10.2514/2.1787
- [23] Haertig, J., Havermann, M., Rey, C., and George, A., "PIV Measurements in Mach 3.5 and 4.5 Shock Tunnel Flow," AIAA Paper 2001-0699, 2001.
- [24] Havermann, M., Haertig, J., Rey, C., and George, A., "PIV Measurements in Shock Tunnels," *PIVNet2 Final Workshop*, DLR Institute of Aerodynamics and Flow Technologie, Göttingen, Germany, 7–8 Sept. 2006.
- [25] Schäfer, H. J., "Application de l'Anémométrie Laser aux Jets de Chambre de Combustion," ISL CO 210/83, 1983.
- [26] George, A., "L'Interférométrie Différentielle. Un Outil Polyvalent Pour le Diagnostic des écoulements," ISL NI 903/2004, 2004.
- [27] Bailly, C., and Comte-Bellot, G., *Turbulence*, 1st ed., CNRS Editions, Paris, 2003, ISBN: 2-271-06008-7.
- [28] Brenner, P., "Three-Dimensional Aerodynamics with Moving Bodies Applied to Solid Propulsion," AIAA Paper 1991–2304, 1991.
- [29] Pollet, M., and Monnaie, C., "A High-Reynolds Model for Turbulence and Heat Transfer in Propulsive Flows," AIAA Paper 1993–2901, 1993.
- [30] Baudin, D., Getin, N., Sourgen, F., and Haertig, J., "Etude de Caractérisation Expérimentale par Mesures Piv D'écoulements Supersoniques Confinés dans un Conteneur de Missile à Lancement Vertical," French-German Research Institute of Saint-Louis, 5 rue du Général Cassagnou, 68100 Saint-Louis, France, ISL S-RV 214/2007, 2007.